SCIENTIFIC REPORTS

OPEN

SUBJECT AREAS:
BATTERIES
SYNTHESIS AND PROCESSING

Received
19 November 2013

Accepted
11 March 2014

Published
26 March 2014

Correspondence and requests for materials should be addressed to Y.L. (liuyong7@mail.sysu.edu.cn)

Constructing hierarchical submicrotubes from interconnected TiO_2 nanocrystals for high reversible capacity and long-life lithium-ion batteries

Ling Xin[1,3], Yong Liu[1], Baojun Li[1], Xiang Zhou[1], Hui Shen[1], Wenxia Zhao[2] & Chaolun Liang[2]

[1]School of Physics and Engineering, State Key Laboratory of Optoelectronic Materials and Technologies, Sun Yat-sen University, Guangzhou 510275, China, [2]Instrumental Analysis & Research Center, Sun Yat-sen University, Guangzhou 510275, China, [3]College of Mechanical and Electrical Engineering, Shenyang Aerospace University, Shenyang, 110136, China.

Here, we report a facile hydrothermal approach for synthesizing anatase TiO_2 hierarchical mesoporous submicrotubes (ATHMSs) with the aid of long-chain polymer as soft template. The TiO_2 nanocrystals, with sizes of 6–8 nm, are well interconnected with each other to build tubular architectures with diameters of 0.3–1.5 μm and lengths of 10–25 μm. Such highly porous structures give rise to very large specific surface area of 201.9 $m^2 g^{-1}$ and 136.8 $m^2 g^{-1}$ for the as-prepared and annealed samples, respectively. By using structurally stable ATHMSs as anode materials for lithium-ion batteries, they exhibited high reversible capacity, long cycling life and excellent cycling stability. Even after 1000 cycles, such ATHMS electrodes retained a reversible discharge capacity as high as 150 mAh g^{-1} at the current density of 1700 mA g^{-1}, maintaining 92% of the initial discharge capacity (163 mAh g^{-1}).

TiO_2 materials have been extensively studied since it is suitable for a wide range of applications such as lithium-ion batteries (LIBs), photocatalysis, photocleavage of water, chemical sensors, and dye-sensitized solar cells[1,2]. For example, TiO_2 has been considered as a promising substitute of commercial graphite anode materials for LIBs since it operates at a relatively high lithium insertion/extraction voltage (1.5–1.8 V *vs* Li/Li^+), which may efficiently avoid the formation of solid electrolyte interface (SEI) layers and lithium plating on the anode, and therefore enabling enhanced safety of the batteries. In addition, the volume change of TiO_2 is negligible (less than 4%) during lithium ion intercalation/deintercalation processes, which affords TiO_2 outstanding structure stability, and hence ensuring extended cycle life[2–5].

To further improve LIB performance, scientific breakthroughs are still required to simultaneously minimize the four primary resistances during charge and discharge: (i) ion transport in the electrolyte, (ii) ion transport in the electrode, (iii) electrochemical reactions in the electrode, and (iv) electron conduction in the electrode and current collector[6]. It is widely accepted that approaches for solving these problems are strongly related to nanoengineer active electrode materials with desired morphologies, specific surface area, size and crystallinity. As a result, TiO_2 materials with different morphologies such as nanoparticles, nanowires/rods, nanosheets, nanobelts, nanofibers, nanotubes, and mesoporous solid/hollow microspheres have been reported in recent years[7]. Among them, porous structures, such as nanotubes and mesoporous hollow microspheres, are very attractive structures based on above consideration[5]. For example, TiO_2 nanotubes show unique rate capabilities for LIBs due to their relatively large specific surface area, shortened diffusion length, and fast electron transport restricted in one dimention[8–12]. Whereas, most reported nanotubes are too small for a moderate amount of electrolyte to penetrate into their tunnels[13]. Furthermore, these nano-scaled materials also reduce the pack density and energy density of the LIBs[14,15]. In addition, the reported submicron-sized tubular geometry, such as hollow fibers and hollow ribbons, which allow for a large lithium-ion flux to wet the hollow space easily, have been obtained by atomic layer deposition or electrospinning technique[13,16,17]. However, the specific surface area would decrease with the increasing size from nanoscale to submicron scale. Moreover, hierarchical hollow micro/submicro-spheres are also considered as very promising alternative structures since these structures combine advantages of primary nano-sized and secondary micron-sized structures, respectively[18–20]. Firstly, the robust and micron/submicron hollow structure can both prevent the aggregation and provide high tap density. Secondly, the

micron/submicron hollow structure or macropores can also act as a buffering reservoir of electrolyte so as to minimize the transport resistances. Thirdly, the nano-sized primary particles can facilitate ionic transport by reducing the diffusion length. Finally, the formed mesoporous structures can offer large surface area, which, as a result, ensure more interfacial contact between the active material and the electrolyte. Unfortunately, it is usually a slow and ineffective process for the diffusion of lithium-ion into the interior of hollow sphere due to the closed shell structures. Interestingly, the hollow sphere with an opening hole fabricated by Huang[21] is particularly promising. However, the relatively low electrical transport among neighboring microspheres still significantly limits the rate performance of LIBs[6,22].

To tackle these issues, we present a self-assembled anatase TiO_2 hierarchical mesoporous submicrotube (ATHMS) electrode architecture. In this architecture, the ultrasmall anatase TiO_2 nanocrystals were well interconnected with each other to build mesoporous tubular architectures. As shown in Figure 1, this unique structure simultaneously combines many important features of macro-/mesoporous and tubular structure and thus provides: (i) the longitudinal pathways of submicron-sized tubular structure that would decrease electrolyte diffusion resistance and serve as a buffering reservoir of electrolyte, (ii) mesoporous feature that offers a short solid-phase ion diffusion length and rapid ion transport, (iii) a large electrode surface area and sufficient electrochemical reactions in the electrode, and (iv) one dimensional interconnected nanocrystal network for efficient electron transport. Thus, this unique structure can simultaneously handle all four resistances mentioned above, which enables a high reversible capacity, long cycling life, and excellent cycling stability. For instance, such an electrode retained reversible discharge capacities as high as 150 mAh g^{-1} at current density of 1700 mA g^{-1} (5 C, C rate was based on the theoretical specific capacity of TiO_2, where a 1C rate corresponded to a current density of 335 mA g^{-1}) even after 1000 cycles, maintaining 92% of the initial discharge capacity (163 mAh g^{-1}).

Results

The morphologies and crystal structure of the as-prepared samples were examined by field emission scanning electron microscopy (FESEM), X-ray diffraction (XRD), and Raman, respectively. As shown in FESEM images of Figure 2a–c, the as-synthesized submicrotubes, with diameters of 0.3–1.5 μm and lengths of 10–25 μm, are large-scale and monodisperse. Figure 2d shows the XRD patterns of the same sample, and all the diffraction peak positions agree well with that of the anatase phase of TiO_2 (JCPDS 84-1286). The anatase phase of the as-prepared samples was further confirmed by Raman spectrum measurement. As seen in Figure S1, the characteristic Raman modes of anatase TiO_2 are observed at 148 (Eg), 399 (B1g), 516 (A1g or B1g) and 639 cm^{-1} (Eg), respectively[8].

The morphology and crystal structure of ATHMSs were further confirmed by transmission electron microscopy (TEM) images (Figure 3). As revealed in Figure 3a, the products show a strong contrast in the degree of brightness, with dark edges and a lighter center, indicating the formation of tubular structure. The inset of Figure 3a shows the selective area electron diffraction (SAED) patterns of ATHMSs. Consistent with XRD analysis, the diffraction rings can be indexed to (101), (004), (200), and (105) planes of anatase phase, indicating the polycrystalline nature of ATHMSs. As shown from HRTEM image in Figure 3b, the wall of as-prepared ATHMS is composed of numerous ultrasmall nanocrystallites with sizes of 6–8 nm, which are well interconnected with each other to form abundant mesopores. Moreover, the measured distance of 0.35 nm between the adjacent lattice fringes can be assigned to (101) plane of the anatase TiO_2 (the inset of Figure 3b).

The thermogravimetric (TG) analysis is shown in Figure S2, it reveals that as-prepared TiO_2 sample only contains 12.8 wt% of organic species, and the weight loss of 2.9 wt% below 100 °C can be attributed to the evaporation of adsorbed moisture. In spite of the well crystallization of as-prepared sample, further heat treatment is necessary to remove the residual organic species. It can be seen from the TG curve that the residual organic species could be removed completely after annealing at 400 °C. Therefore, our ATHMSs were calcined at 400°C for 3 h before it was used as anode material in LIBs.

Figure 4 shows the N_2 adsorption–desorption isotherms (77 K) and pore size distribution of the ATHMS samples before and after calcination. The isotherm with an adsorption–desorption hysteresis is between type II and type IV according to the international union of pure and applied chemistry (IUPAC) classification[23,24]. A steep increase in the amount of nitrogen adsorbed is clearly observed at high relative pressures ($P/P^\circ > 0.8$), suggesting the presence of macropores (>50 nm), which corresponds to submicron-sized tubular structure observed in SEM and TEM (Figure 2a–c and Figure 3a). Besides, H3 hysteresis loop reveals that mesopores (2–50 nm) exist in both as-prepared and annealed ATHMSs. The Barrett–Joyner–Halenda (BJH) pore size distributions derived from the desorption branch exhibit that pore size of the as-prepared and annealed ATHMS samples centered at 8.39 nm and 15.39 nm,

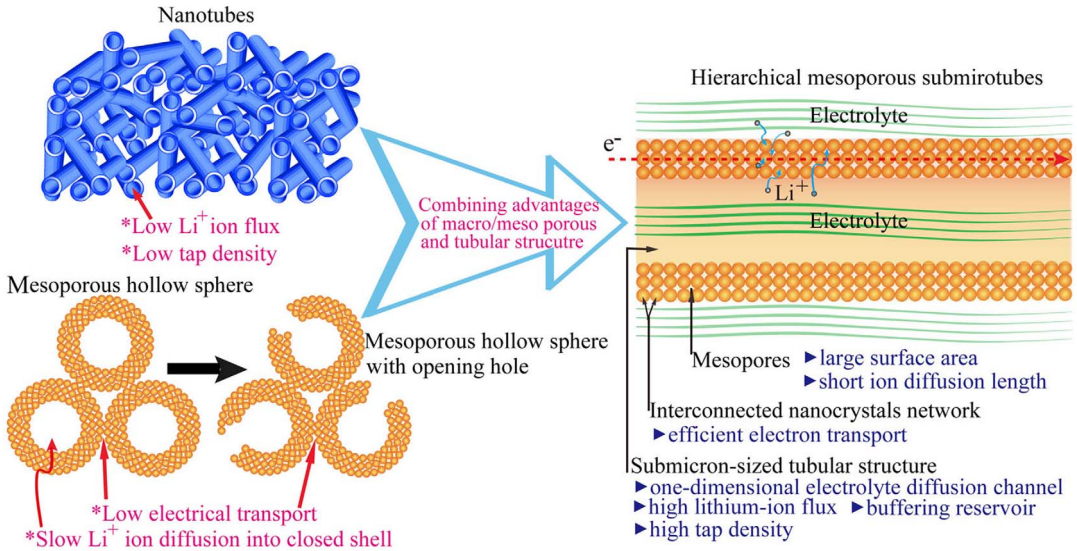

Figure 1 | Schematic illustration of ATHMS combining advantages of macro/meso porous and tubular structures.

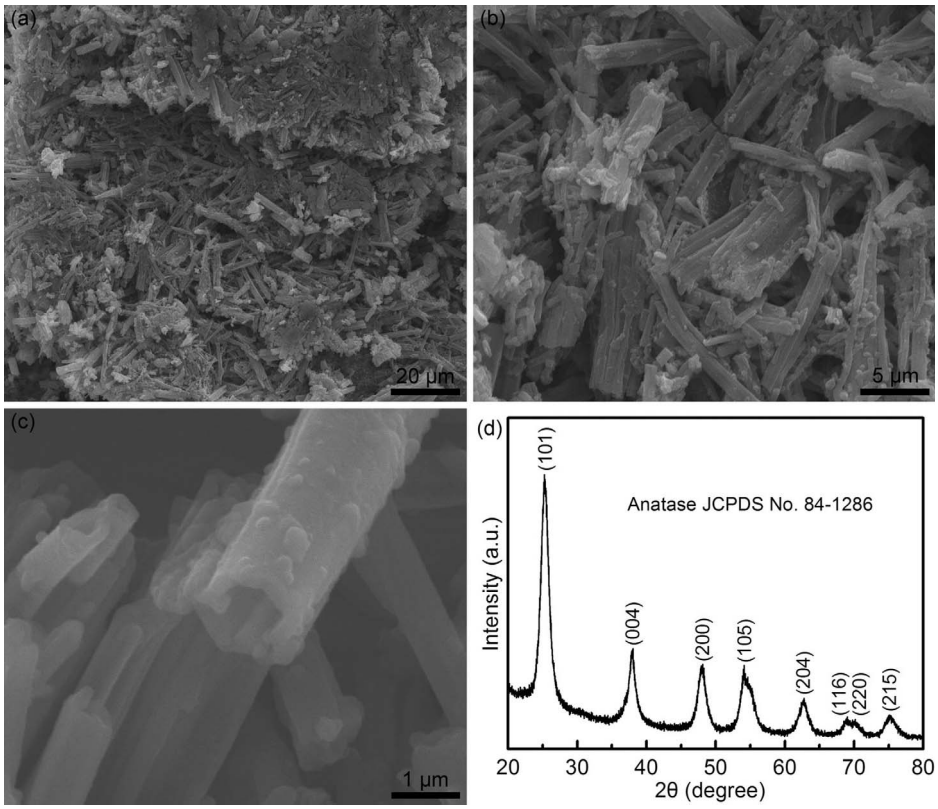

Figure 2 | (a)–(c) FESEM images and (d) XRD pattern of the ATHMSs obtained by hydrothermal treatment at 180 °C for 12 h.

respectively (inset of Figure 4). As calculated by the Brunauer-Emmett-Teller (BET) method, such porous structures give rise to very high specific surface area of 201.9 $m^2\ g^{-1}$ and 136.8 $m^2\ g^{-1}$ for the as-prepared and annealed ATHMS samples, respectively. Therefore, the large surface area of ATHMSs obtained here can provide more surface active sites for electrochemical reaction of electrode materials, making the charge transport and ion diffusion more efficient.

It is important for TiO_2 materials to remain their morphology and structure after the heat treatment while they are applied in LIBs. Figure 5a–c show the SEM images, XRD, TEM and SAED of ATHMS after sintering at 400 °C for 3 h. Benefiting from the relatively stable structure, the ATHMSs can withstand annealing process without collapse or deformation. And the anatase phase was still maintained after calcination. Furthermore, the HRTEM image (Figure 5d) clearly shows the polycrystalline texture of the mesoporous tube walls assembled from interconnected nanoparticles with diameters of 6–9 nm.

Figure 6a shows the representative cyclic voltammograms (CVs) of the LIBs made with ATHMSs. Two obvious current peaks are observed at 1.6 V and 2.1 V, which attributed to the insertion/extraction of Li^+ ions at anode and cathode, respectively. The ratio of cathodic to anodic peak current intensity for the first scan is nearly 1 due to the equal extent of insertion/extraction of Li^+ ions in ATHMSs, indicating superior charge transfer and ion diffusion kinetics behavior. Figure 6b shows the first charge-discharge voltage profiles of the ATHMS electrodes in the first cycle at different current rates. It is found that the potential difference between the discharge

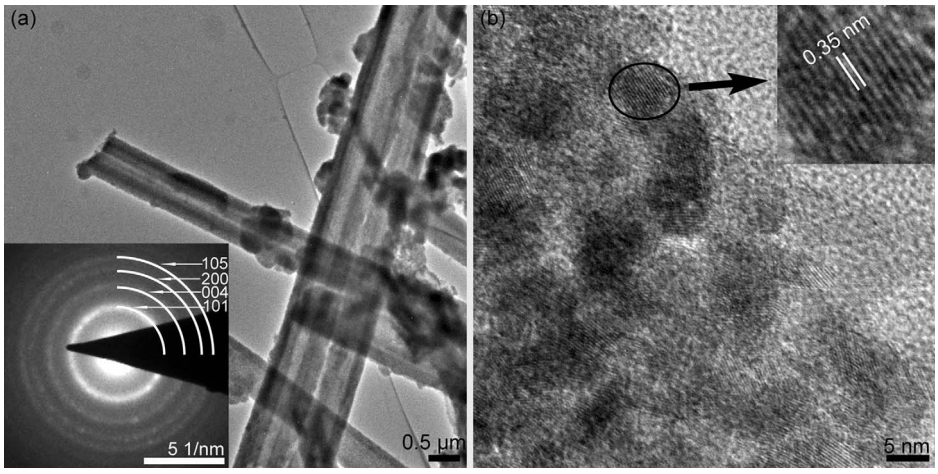

Figure 3 | TEM images and corresponding SAED pattern of the ATHMSs prepared by hydrothermal treatment at 180 °C for 12 h. (a) Low magnification TEM image and the SAED pattern (the inset). (b) HRTEM and an enlarged HRTEM taken from the solid circle in Figure 3b.

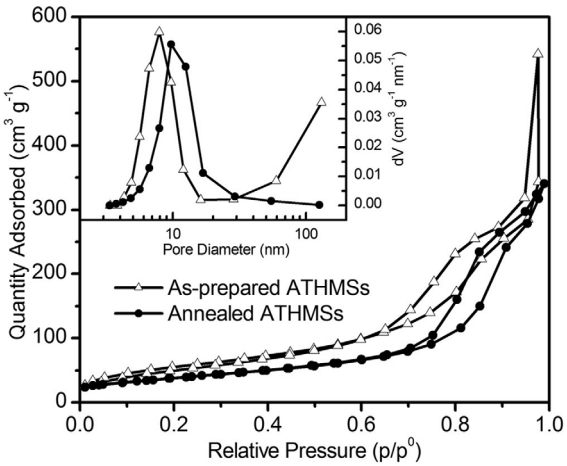

Figure 4 | N_2 adsorption-desorption isotherms for as-prepared and annealed ATHMS samples, respectively. The inset shows their corresponding pore size distribution.

and charge plateaus increased with the increase of the current rate, which maybe due to the polarization of the electrode at high current density[25]. At different current density of 0.5 C, 1 C, 2.5 C, and 5 C (here 1 C = 335 mA g^{-1}), the ATHMS electrodes delivered first discharge/charge capacities of 280/239, 231/199, 181/172, and 163/150 mAh g^{-1}, respectively, implying much lower initial irreversible capacity loss (ICL) values of 14.6%, 13.9%, 5.0%, and 8.0%. Furthermore, ICL values in the first cycle, ranging from 5% to 10%, were reproducibly observed for another four ATHMS electrodes at current density of 850 mA g^{-1} (2.5 C), as shown in Figure S3. The ICL values in the first circle reported here are lower than that of most of other anatase TiO_2 electrodes[8,13,16–19,26]. The lower ICL values indicate a higher reversible capacity to meet the requirements of practical applications in the future. The cyclic stability of the ATHMS electrode was further investigated at different current rates, as shown in Figure 6c. After 50 cycles at the current rate of 0.5, 1, 2.5, and 5 C, our ATHMS electrodes delivered high discharge capacities of 218, 184, 167, and 164 mAh g^{-1}, respectively. Remarkably, they still retained a reversible discharge capacity as high as 221 mAh g^{-1} at 0.5 C, 184 mAh g^{-1} at 1 C, 169 mAh g^{-1} at 2.5 C, 162 mAh g^{-1} at 5 C after 100 cycles, respectively, implying negligible capacity fading from 50 to 100 cycles. In addition, we have repeatedly obtained high capacities and good capacity retention of our ATHMS electrodes by using another four ATHMS electrodes at the current density of 2.5 C, as shown in Figure S3 and Figure S4. These ATHMS electrodes showed discharge capacities of 201, 200, 184, and 174 mAh g^{-1}, and maintaining 87%, 84%, 88%, and 87% of the initial discharge capacity after 100 cycles, respectively. The discharge capacity retention and cycling stability for ATHMS electrodes after 50 or 100 cycles reported here are higher than that of other TiO_2 anatase tubular structures[8–10,13,17], mesoporous hollow sphere[18–21], and even that treated with conductive pathways such as TiO_2/graphene[27,28], and mesoporous TiO_2:RuO_2 composite electrodes[29] while tested under similar conditions. In particular, the discharge capacities only decreases slightly to 158 mAh g^{-1} at 2.5 C, and 150 mAh g^{-1} at 5 C after 1000 cycles, corresponding to 87%, and 92% of their initial capacity, respectively (Figure 6c). Furthermore, the Coulombic efficiency shown is nearly 100% at each cycle at 5 C charge–discharge rates (Figure S5). Obviously, the ATHMS electrodes exhibit high reversible capacity, excellent cycling stability and long circling life, indicating a very promising candidate for LIBs. The rate performance of the ATHMSs and commercial anatase TiO_2 nanoparticles (25 nm) at 0.25–5 C rates was also investigated, as shown in Figure 6d. Compared to anatase TiO_2 nanoparticles, the ATHMSs exhibit excellent rate capability at all current rates, which maybe due to the unique macro/mesoporous and tubular structures ensuring fast electron transfer and high Li^+ ion diffusion rates. After this

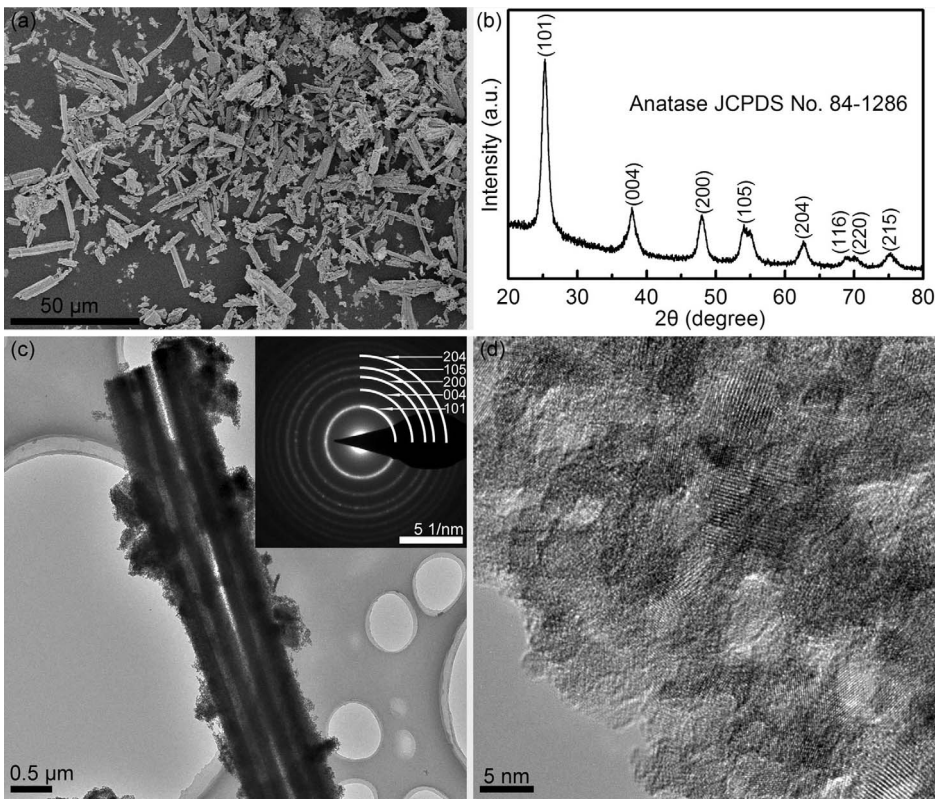

Figure 5 | (a) FESEM image (b) XRD pattern, (c) TEM image and corresponding SAED pattern (the inset), and (d) HRTEM image of the ATHMS samples after calcination at 400 °C for 3h.

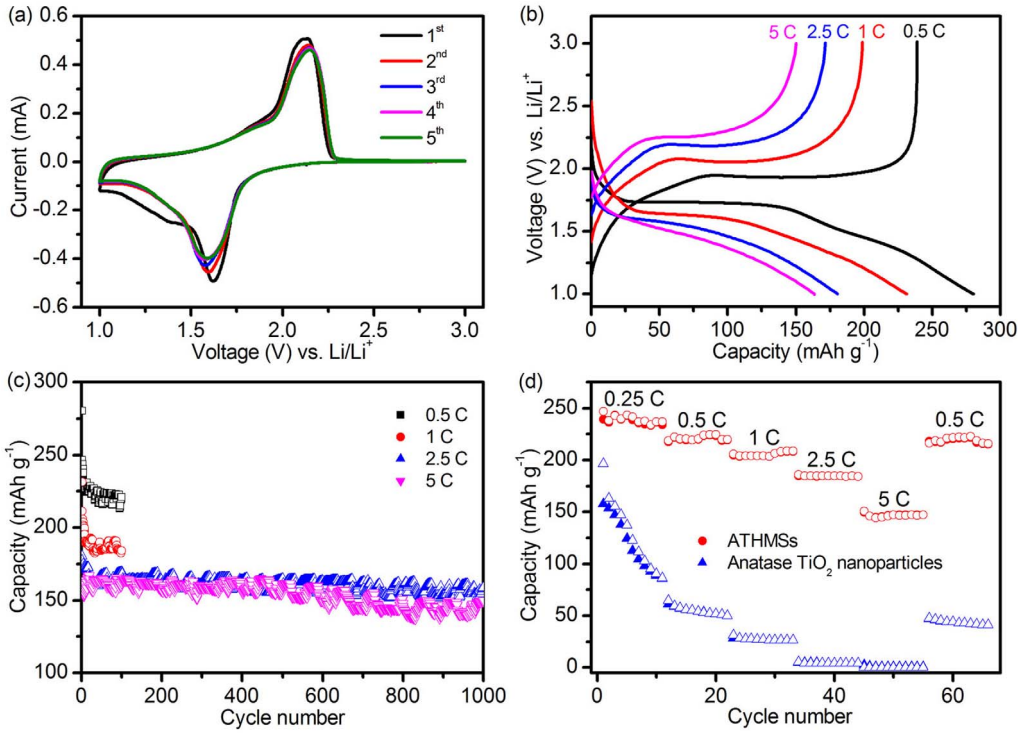

Figure 6 | (a) CVs of the ATHMS electrode from the first cycle to the fifth cycle at a scan rate of 0.2 mV s^{-1}. (b) Galvanostatic charge–discharge profiles of ATHMS electrodes at different current rate of 170 mA g^{-1} (0.5C), 340 mA g^{-1} (1 C), 850 mA g^{-1} (2.5 C), and 1700 mA g^{-1} (5 C), respectively. (c) Cycling performance of the ATHMS electrodes at the different C rates. (d) Specific capacity of the ATHMS and anatase TiO_2 nanoparticles at different C rates. All of measurements were conducted in voltage range of 1.0–3.0 V.

high-rate charge–discharge process, a stable capacity of 222 mAh g^{-1} could be supplied again when the current rate is reduced back to 0.5 C, indicating the high reversibility of the electrode materials. The excellent rate capability exhibited by ATHMSs suggests them as promising anode material for LIBs with large power densities.

The electrochemical impedance spectroscopy (EIS) measurements were thus undertaken to reveal the kinetic process of lithium ion diffusion and electron transfer of the ATHMS electrodes. For comparison, the LIBs consisting of commercial anatase TiO_2 nanoparticles were also investigated. Figure 7 illustrates the Nyquist plots of ATHMS and anatase TiO_2 nanoparticle based LIBs before galvanostatic discharging/charging and after 100 cycles at a current rate of 170 mA g^{-1} (0.5 C). Obviously, they exhibit single semicircles for fresh cells or two partially overlapped semicircles for cycled cells, and followed by the appearance of strait line Warburg-type region from high to low frequency. The Warburg-type straight lines of fresh cells made with ATHMS and anatase TiO_2 nanoparticles show an angle approaching 90° to the Z′-axis, which indicated that detectable lithium intercalation did not occur for fresh cells, and they decreased closely to an angle of 45° to the Z′-axis after 100 cycles, which is characteristic of Li-ion diffusion through the homogeneous single anatase phase of the electrodes[30–32]. An equivalent circuit for these LIBs was used to fit the Nyquist plots, as depicted in the inset of Figure 7. Here, R_e represents the combined resistance of electrolyte and cell components. $R_{(sf+ct)}$ depicts the surface film (sf) and charge transfer resistance (ct). R_b is the bulk (b) resistance. The constant phase elements $CPE_{(sf+dl)}$ is due to the surface film and double layer (dl) capacitance, whereas CPE_b refers to bulk capacitance. In addition, W_s and C_i represent the Warburg impedance and interclation capacitance. More detailed discussion of this equivalent circuit is found in the references[32–34]. According to the fitted values for fresh cells, R_{sf} (162.8 Ω) for ATHMS electrode is much smaller than that (182.0 Ω) for the anatase TiO_2 nanoparticle electrode. After 100 charge-discharge cycles, the $R_{(sf+ct)}$ (143.9 Ω) of ATHMS electrode is also smaller than that (165.5 Ω) of anatase TiO_2 nanoparticle electrode. The low $R_{(sf+ct)}$ of ATHMS electrode demonstrates the good electronic contact and effective charge transport are maintained after repeated Li^+ ions insertion and extraction process, as compared to anatase TiO_2 nanoparticle electrode. Furthermore, the diameters of the semicircle and angle of Warburg-type to the Z′-axis for cycled ATHMS and anatase cells have lower values than that of fresh ATHMS and anatase cells, which are consistent with that reported in the references[31]. Therefore, the outstanding rate and cycling performance of ATHMS could be attributed to the synergistic effect of the enhanced electron transport and Li^+ ion diffusion in ATHMS electrodes.

To reveal why the lithium storage of these ATHMS electrodes is stable in this work, the morphology of ATHMSs was further compared before galvanostatic discharging/charging and after completion of 1000 charge/discharge cycles at a current rate of 1700 mA g^{-1} (Figure 8). Obviously, these tubular structures are well preserved even under the current density as high as 1700 mA g^{-1} for 1000 cycles (Figure 8b), which is of great significance for keeping the capacity. Therefore, the excellent reversible capacity of ATHMS could be due to their stable and unique structural features. The one-dimensional submicron-sized tubular structure may provide fast diffusion channel for electrolyte due to the lower diffusion resistance and reservoir for the electrolyte. Whereas, the highly porous framework is considered to make significant contributions not only to increasing the contact area between the electrolyte/anode materials but also to facilitating penetration of the electrolyte into the inner region of active materials. In addition, the interconnected nanocrystal network may shorter diffusion lengths for both electrons and ion transport.

Discussion

In summary, a mild facile hydrothermal method was used to fabricate well-defined anatase TiO_2 hierarchical mesoporous submicrotubes

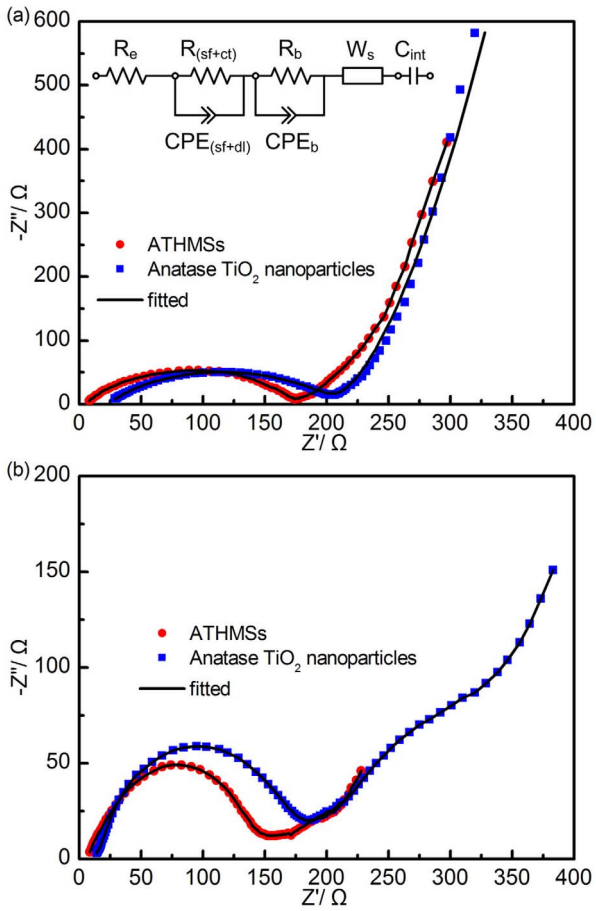

Figure 7 | EIS of ATHMS and anatase TiO_2 nanoparticle based LIBs (a) before galvanostatic discharging/charging and (b) after 100 cycles at a current rate of 170 mA g^{-1}. The equivalent circuit used to fit the experimental data is shown as an inset. Dots represent the experimental data, and solid curves represent the fitted curve.

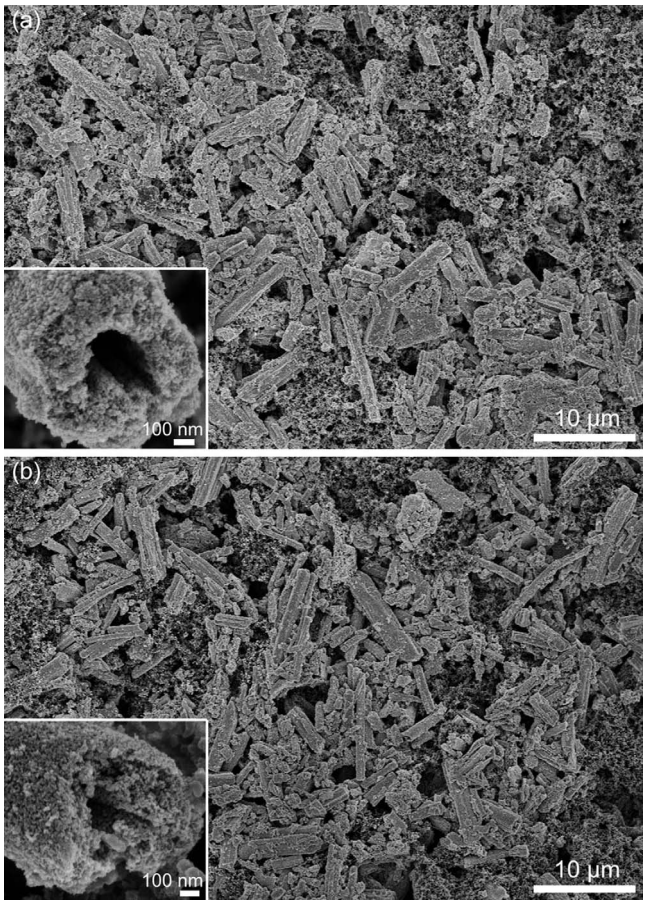

Figure 8 | FESEM images of the ATHMS electrode (a) before galvanostatic discharging/charging and (b) after completion of 1000 discharge-charge cycles at a current rate of 1700 mA g^{-1}. The insets in (a) and (b) are high magnification of ATHMS.

by using long-chain polymer as soft template. By taking advantage of this unique electrode architecture, it delivered a reversible discharge capacity as high as 150 mAh g^{-1} at a current density rate of 1700 mA g^{-1} and good reversibility with cycling efficiency of 92% after 1000 cycles. This demonstrates that constructing TiO_2 hierarchical mesoporous submicrotubes with "macroporous", "mesoporous", and "one-dimensional" characteristics is a significant approach to enhance electrode electrochemical properties. Benefiting from such unique structural features, the products can serve as superior active materials in high-performance lithium-ion batteries application. This work demonstrates the promising use of hierarchically mesoporous tubular structure in high-performance LIB applications.

Methods

Material synthesis. All chemical reagents were commercially available and used without further purification. In a typical synthesis, 0.6 g polyacrylamide (A.R., molecular weight: ≥5 million, Kermel), was added to 60 mL of deionized water under vigorous stirring for 10 min. Then, 0.3 g Titanium(IV) oxysulfate-sufuric acid hydrate (93%, Aladdin) was added to this solution and stirred for 30 min. The reaction solution was then transferred to a 100 mL Teflon-lined autoclave and then hydrothermally heated at temperature of 180 °C for 12 h. Afterward, the autoclave was taken out and cooled naturally to room temperature. After that, the white precipitate was collected and washed with ethanol and deionized water for several times, and dried at 60 °C for 24 h. Finally, the obtained ATHMS samples were calcined at 400 °C for 3 h with a heating rate of 1 °C min^{-1} to remove residual organics before it was used as anode material in LIBs.

Characterization. The product morphology was examined using a high-resolution field emission scanning electron microscopy (FESEM, JSM-7600F, JEOL). The crystal structure of the samples was analyzed by using X-ray diffraction (XRD, D8 Advance, Bruker) with Cu Kα radiation. Raman spectra analysis was conducted from 100 to 1000 cm^{-1} using an Almega Dispersive Raman system (Renishaw inVia) and a Nd:YAG intracavity doubled laser operating at 514.5 nm. Transmission electron microscopy (TEM) observations were carried out with a high resolution transmission electron microscope (FEI Tecnai G2 F30) operating at 300 kV. The thermogravimetric (TG) analysis was carried out by using a thermogravimeter (TG209, Netzsch Instruments, Germany) from 30 to 800 °C at a linear heating rate of 10 °C min^{-1}. The pore characteristics and surface area were analyzed by a nitrogen adsorption–desorption apparatus (ASAP 2020M, Micromeritics).

The electrochemical measurements. The electrochemical measurements were performed using two-electrode CR2025-type coin cells with pure lithium metal serving as both the counter and reference electrodes at room temperature. The working electrode was composed of active material (e.g., ATHMSs), conductivity agent (carbon black, Super-P-Li), and binder (polyvinylidene difluoride, PVDF, Aldrich) in a weight ratio of 70 : 20 : 10 in N-methyl-2-pyrrolidone (NMP). The geometrical area of the electrode was 1.54 cm^2 and the mass loading of active material in our working electrode was controlled at about 1.2–2 mg. The electrolyte used was 1.0 M LiPF6 in a 1 : 1 (w/w) mixture of ethylene carbonate-diethyl carbonate (Technologies, USA). A porous membrane (Celgard 3400) was used as a separator. Cell assembly was carried out in an Argon-filled glovebox with moisture and oxygen concentrations below 1.0 ppm. The cyclic voltammetry (CV) and electrochemical impedance spectroscopy (EIS) measurements were performed on an electrochemical workstation (CHI760C, CH Instruments) at room temperature. Galvanostatic charge/discharge cycling was carried on with a battery testing system (NEWARE) with a voltage window of 1–3 V *vs.* Li^+/Li at different current rates of 0.25 C, 0.5 C, 1 C, 2.5 C, 5 C, respectively, where 1 C = 335 mA g^{-1}. Reference experiments were performed by using commercial anatase TiO_2 nanoparticles (25 nm, Aladdin Chemistry Co. Ltd) as anode material.

1. Chen, X. & Mao, S. S. Titanium dioxide nanomaterials: synthesis, properties, modifications, and applications. *Chem. Rev.* **107**, 2891–2959 (2007).

2. Reddy, M. V., Subba Rao, G. V. & Chowdari, B. V. R. Metal oxides and oxysalts as anode materials for Li ion batteries. *Chem. Rev.* **113**, 5364–5457 (2013).
3. Chen, Z., Belharouak, I., Sun, Y. K. & Amine, K. Titanium-based anode materials for safe lithium-ion batteries. *Adv. Funct. Mater.* **23**, 959–969 (2013).
4. Deng, D., Kim, M. G., Lee, Y. J. & Cho, J. Green energy storage materials: Nanostructured TiO_2 and Sn-based anodes for lithium-ion batteries. *Energy Environ. Sci.* **2**, 818–837 (2009).
5. Su, X. *et al*. Advanced titania nanostructures and composites for lithium ion battery. *J Mater Sci.* **47**, 2519–2534 (2012).
6. Zhang, H., Yu, X. & Braun, P. V. Three-dimensional bicontinuous ultrafast-charge and -discharge bulk battery electrodes. *Nature Nanotech.* **6**, 277–281 (2011).
7. Jiang, C. & Zhang, J. Nanoengineering titania for high rate lithium storage: a review. *J. Mater. Sci. Technol.* **29**, 97–122 (2013).
8. Xu, J., Jia, C., Cao, B. & Zhang, W. F. Electrochemical properties of anatase TiO_2 nanotubes as an anode material for lithium-ion batteries. *Electrochem. Acta* **52**, 8044–8047 (2007).
9. He, B. L., Dong, B. & Li, H. L. Preparation and electrochemical properties of Ag-modified TiO_2 nanotube anode material for lithium-ion battery. *Electrochem. Commun.* **9**, 425–430 (2007).
10. Han, H. *et al.* Dominant factors governing the rate capability of a TiO_2 nanotube anode for high power lithium ion batteries. *ACS Nano* **6**, 8308–8315 (2012).
11. Zhou, Y. K., Cao, L., Zhang, F. B., He, B. L. & Li, H. L. Lithium insertion into TiO_2 nanotube prepared by the hydrothermal process. *J. Electrochem. Soc.* **150**, A1246–A1249 (2003).
12. Wei, W. *et al*. High energy and power density TiO_2 nanotube electrodes for 3D Li-ion microbatteries. *J. Mater. Chem. A.* **1**, 8160–8169 (2013).
13. Kim, S. W. *et al*. Fabrication and electrochemical characterization of TiO_2 three-dimensional nanonetwork based on peptide assembly. *ACS Nano* **3**, 1085–1090 (2009).
14. Xiao, J., Zheng, J., Li, X., Shao, Y. & Zhang, J. G. Hierarchically structured materials for lithium batteries. *Nanotechnology* **24**, 424004 (2013).
15. Guo, B., Ruan, H., Zhen, C., Fei, H. & Wei, M. Hierarchical $LiFePO_4$ with a controllable growth of the (010) facet for lithium-ion batteries. *Sci. Rep.* **3**, 2788 (2013).
16. Tang, K., Yu, Y., Mu, X., van Aken, P. A. & Maier, J. Multichannel hollow TiO_2 nanofibers fabricated by single-nozzle electrospinning and their application for fast lithium storage. *Electrochem. Commun.* **28**, 54–57 (2013).
17. Han, H. *et al*. Nitridated TiO_2 hollow nanofibers as an anode material for high power lithium ion batteries. *Energy Environ. Sci.* **4**, 4532–4536 (2011).
18. Xiao, L. *et al*. Preparation and electrochemical lithium storage features of TiO_2 hollow spheres. *J. Power Sources* **238**, 197–202 (2013).
19. Ma, Y., Ji, G., Ding, B. & Lee, J. Y. Facile solvothermal synthesis of anatase TiO_2 microspheres with adjustable mesoporosity for the reversible storage of lithium ions. *J. Mater. Chem.* **22**, 24380–24385 (2012).
20. Yu, L., Wu, H. B. & Lou, X. W. Mesoporous $Li_4Ti_5O_{12}$ hollow spheres with enhanced lithium storage capability. *Adv. Mater.* **25**, 2296–2300 (2013).
21. Ding, S., Lin, T., Wang, Y., LÜ, X. & Huang, F. New facile synthesis of TiO_2 hollow sphere with an opening hole and its enhanced rate performance in lithium-ion batteries. *New J. Chem.* **37**, 784–789 (2013).
22. Guo, Y. G., Hu, J. S. & Wan, L. J. Nanostructured materials for electrochemical energy conversion and storage devices. *Adv. Mater.* **20**, 2878–2887 (2008).
23. Kruk, M. & Jaroniec, M. Gas Adsorption characterization of ordered organic-inorganic nanocomposite materials. *Chem. Mater.* **13**, 3169–3183 (2001).
24. Ma, T. Y., Zhang, X. J. & Yuan, Z. Y. Hierarchical meso-/macroporous aluminum phosphonate hybrid materials as multifunctional adsorbents. *J. Phys. Chem. C.* **113**, 12854–12862 (2009).
25. Saravanan, K., Ananthanarayanan, K. & Balaya, P. Mesoporous TiO_2 with high packing density for superior lithium storage. *Energy Environ. Sci.* **3**, 939–948 (2010).
26. Chen, J. S. *et al*. Constructing hierarchical spheres from large ultrathin anatase TiO_2 nanosheets with nearly 100% exposed (001) facets for fast reversible lithium storage. *J. AM. CHEM. SOC.* **132**, 6124–6130 (2010).
27. Xin, X. *et al*. Scalable synthesis of TiO_2/graphene nanostructured composite with high-rate performance for lithium ion batteries. *ACS NANO* **6**, 11035–11043 (2012).
28. Li, D. *et al*. TiO_2 nanoparticles on nitrogen-doped graphene as anode material for lithium ion batteries. *J. Nanopart. Res.* **15**, 1674 (2013).
29. Guo, Y., Hu, Y., Sigle, W. & Maier, J. Superior electrode performance of nanostructured mesoporous TiO_2 (anatase) through efficient hierarchical mixed conducting networks. *Adv. Mater.* **19**, 2087–2091 (2007).
30. Funabiki, A., Inaba, M. & Ogumi, Z. A. c. impedance analysis of electrochemical lithium intercalation into highly oriented pyrolytic graphite. *J. Power Sources* **68**, 227–231 (1997).
31. Li, G., Zhang, Z., Peng, H. & Chen, K. Mesoporous hydrogenated TiO_2 microspheres for high rate capability lithium ion batteries. *RSC Adv.* **3**, 11507–11510 (2013).
32. Reddy, M. V., Madhavi, S., Subba Rao, G. V. & Chowdari, B. V. R. Metal oxyfluorides $TiOF_2$ and NbO_2F as anodes for Li-ion batteries. *J. Power Sources* **162**, 1312–1321 (2006).
33. Reddy, M. V., Subba Rao, G. V. & Chowdari, B. V. R. Nano-$(V_{1/2}Sb_{1/2}Sn)O_4$: a high capacity, high rate anode material for Li-ion batteries. *J. Mater. Chem.* **21**, 10003–10011 (2011).
34. Reddy, M. V. *et al*. Preparation and electrochemical studies of electrospun TiO_2 nanofibers and molten salt method nanoparticles. *Electrochimica Acta* **55**, 3109–3117 (2010).

Acknowledgments

This work was financially supported by the National Natural Science Foundation of China (Grant 51272294), the National Basic Research Program of China (Grant 2012CB933704) and the Scientific Research Foundation for the Returned Overseas Chinese Scholars, State Education Ministry (JYB201301).

Author contributions

Y.L. and L.X. proposed and designed the experiments. L.X. carried out the experiments (synthesis and electrochemical tests) and characterizations. Y.L. and L.X. wrote the paper. B.J.L., X.Z. and H.S. provide scientific advice. W.X.Z. and C.L.L. conducted the SEM and HRTEM measurements, respectively. All authors read and approved the final manuscript.

Additional information

Supplementary information accompanies this paper at http://www.nature.com/scientificreports

Competing financial interests: The authors declare no competing financial interests.

How to cite this article: Xin, L. *et al.* Constructing hierarchical submicrotubes from interconnected TiO_2 nanocrystals for high reversible capacity and long-life lithium-ion batteries. *Sci. Rep.* **4**, 4479; DOI:10.1038/srep04479 (2014).